Biosensors and Bioelectronics: X 30 (2026) 100783

Contents lists available at ScienceDirect

Biosensors and Bioelectronics: X

journal homepage: www.journals.elsevier.com/biosensors-and-bioelectronics-x

Micromixer-controlled nanoparticle size distribution for biomolecular interaction readouts

İsmail Bütün [a,b,1], Melis Hazal Porsuk [a,b,1], Mine Demir Khan [c], İrem Acar [d], Sibel Çetinel [a,b], Özlem Kutlu [a,b], Havva Funda Y. Acar [c], Ali Koşar [a,b,e,f,*]

[a] Faculty of Engineering and Natural Sciences, Sabancı University, Türkiye
[b] Sabancı University Nanotechnology Research and Application Centre (SUNUM), İstanbul, Türkiye
[c] Department of Chemistry, Koç University, Sarıyer, İstanbul, 34450, Türkiye
[d] Department of Biomedical Science and Engineering, Koç University, Sarıyer, İstanbul, 34450, Türkiye
[e] Center of Excellence for Functional Surfaces and Interfaces for Nano-Diagnostics (EFSUN), Sabancı University, Istanbul, Türkiye
[f] Turkish Academy of Sciences (TÜBA), Çankaya, 06700, Ankara, Türkiye

ARTICLE INFO

Keywords:
Micromixing
Transition flow element (TFU)
Fabrication
Streptavidin
Alpha-fetoprotein

ABSTRACT

The interaction of nanoparticles within the micromixer-assisted microfluidic platforms offers a powerful strategy for controlled biomarker capture by simultaneously enhancing surface-activated binding and transport-limited interactions under laminar flow conditions. In this study, poly(acrylic acid)-coated superparamagnetic iron oxide nanoparticles (SPION) with a number-based hydrodynamic diameter of 13.2 nm and a strong negative zeta potential (−55.3 mV) were synthesized and successfully functionalized with streptavidin and alpha-fetoprotein (AFP)-specific antibodies using EDC/NHS chemistry, achieving a conjugation efficiency of 98%. Protein conjugation resulted in systematic increases in hydrodynamic size and corresponding reductions in zeta potential, confirming effective surface modification. Streptavidin–biotin interactions (0-12.22 ng/mL) and AFP binding (1 pg/mL to 100 ng/mL) were investigated using dynamic light scattering (DLS) and nanoparticle tracking analyzer (NTA) under both conventional incubation conditions and transition flow element (TFU) mediated micromixing conditions. Microfluidic treatment using a TFU micromixer produced concentration-dependent and reproducible nanoparticle size shifts while maintaining a dominant nanoscale population and preventing uncontrolled aggregation. In contrast, incubation-based assays exhibited broader size distributions, irregular trends, and higher inter-experimental variability. Notably, TFU processing enabled linear and measurable size changes at ~1 nM concentration increments (Re = 20), demonstrating controlled binding kinetics and improved reproducibility. These findings present micromixer-assisted microfluidic systems as effective TFU for harnessing controllable, binding-induced nanoparticle size shifts as a reproducible readout for biomolecular interaction, supporting their potential as preprocessing platforms in early-stage biomarker detection workflows.

1. Introduction

The molecular indicators, well-known as biomarkers, have been used to determine the presence of diseases. Many pathological conditions, including cancer, release biomarkers into circulation at defined stages of progression, enabling their use in diagnostic applications (Zhou et al., 2024). A broad range of biosensing platforms, including electrochemical, acoustic, microelectromechanical (MEMS), immunoassay-based, optical, field-effect transistor, and nanopore sensors, magnetic biosensors, and even mass spectrometry, can detect biomarkers (Koohkansaadi et al., 2025; S. P. Mohanty and E. Kougianos, 2006; Turner, 2013). However, despite these various approaches, the reliable detection of the biomarkers remains a challenge, as they often exist at low concentrations within complex biological fluids (Wu and Qu, 2015). In practice, this biological complexity necessitates advanced equipment and experts, which limit using biosensor platforms to specialized laboratory settings. Such limitations hinder widespread clinical practice and restrict timely, precise diagnosis, especially for patients lacking access to well-equipped

This article is part of a special issue entitled: Microfluidic-based sensors published in Biosensors and Bioelectronics: X.

* Corresponding author. Faculty of Engineering and Natural Sciences, Sabancı University, Türkiye.
E-mail address: kosara@sabanciuniv.edu (A. Koşar).

[1] These authors contributed equally to this work.

https://doi.org/10.1016/j.biosx.2026.100783
Received 12 February 2026; Received in revised form 30 March 2026; Accepted 12 April 2026
Available online 22 April 2026

healthcare infrastructure (Bi et al., 2019; Fitzgerald et al., 2022). Therefore, reducing the cost and complexity associated with the detection of cancer-related biomolecular indicators is essential to enable earlier intervention with improved health outcomes.

Advances in micro and nanofabrication technologies have enabled the miniaturization of medical devices, reshaping healthcare by enabling diagnostic platforms that are faster, more affordable, and accessible (Parvin et al., 2025). In this context, point-of-care approaches allow clinicians to perform diagnostic tests using small volumes of sample fluid and without the need for specialized facilities. As a result, this approach shortens the time between sample collection and diagnosis, contributing to lower costs and improved clinical decisions (Adedokun et al., 2024).

Among the most transformative innovations in modern healthcare lie microsystems with micro- and nanostructures, particularly microfluidic platforms, which operate with minimal sample volumes and can deliver the results in a shorter timeframe (Ardila et al., 2024). Beyond miniaturization, microfluidic technologies have reshaped medical diagnostics through their reusability (Sanjay et al., 2020), biocompatibility (Gharib et al., 2022), multitasking potential (Yeo et al., 2011), high sensitivity (Liu et al., 2010), and seamless integration with other technologies (Nge et al., 2013; Yager et al., 2006). For instance, droplet-based microfluidics has enabled complex diagnostic assays to be performed within picoliter-scale droplets, supporting rapid and portable testing (Shi et al., 2024). Similarly, micro-mixing systems serve as highly efficient microreactors, offering applications from nanoparticle synthesis to drug delivery (Saeed et al., 2025). However, to fully utilize the potential of microfluidic platforms, particularly in the detection of low-concentration biomarkers, effective mixing is necessary to overcome the inherent limitations of laminar flow. In this context, micromixers can also function as a preprocessing microfluidic unit (PMU) for fluid and particle manipulation, facilitating biomolecule handling and detection. Such preprocessing capabilities have enabled some of the most profound transformations in cancer-related microfluidic applications (Boussommier-Calleja et al., 2016; Mehta et al., 2022; Ayuso et al., 2022; Zhai et al., 2024).

Micromixers are considered as one of the most important components of microfluidic systems (Nguyen and Wu, 2004). They include channels at the small scale, and laminar flow conditions typically exist so that the streamlines are regular, which limits mixing (Atencia and Beebe, 2005; Squires and Quake, 2005; Han et al., 2024). The absence of turbulence confines mixing to molecular diffusion alone (Ammar et al., 2025). However, micromixers are required to provide rapid and effective mixing based on heat and mass transfer, especially in biomedical applications (Nguyen, 2011). The fundamental goal is to increase the interfacial layer between two different liquids and shorten the mixing length, which is the traveling distance in the microchannel until two liquids are completely mixed (Han et al., 2024; Shahidian and Tahouneh, 2025). Passive micromixers manipulate the flow paths of liquids depending on the channel geometry, guiding them in twisted, zigzag, or spiral patterns with different channel lengths, widths, and heights (Ahmadi et al., 2021; Hessel et al., 2005; Pennella et al., 2012; Soltani et al., 2024). Such geometrical modifications enhance the liquid-liquid interaction and accelerate diffusion for improved mixing performance (Capretto et al., 2011; Suh and Kang, 2010). Active micromixers, on the other hand, use external energy sources, such as electric fields, magnetic forces, acoustic waves, or pressure fluctuation, to accelerate mixing (Bayareh et al., 2020; Soltani et al., 2024). Each approach aims to overcome the limitations of laminar flow and achieve a homogeneous mixture within a short time.

In many nanoparticle-based systems, the variability arises not from binding chemistry but from heterogeneous transport conditions that lead to disordered nanoparticle-analyte encounters. The control of fluid dynamics and mixing conditions can be as important as the surface chemistry in determining the analytical signal (Åberg et al., 2021). Therefore, micromixers can be considered not only as fluid mixing devices but also as tools used to design the nanoparticle interaction environment (Gimondi et al., 2023).

Indeed, cancer diagnosis has emerged as one of the applications most profoundly reshaped by advances in microfluidic technologies, with a diverse array of systems now enabling new strategies for both fundamental research and clinical oncology (Jain and Pandey, 2022; Shah et al., 2024). In all cancer types, therapeutic applications remain extremely challenging, often requiring invasive intervention protocols and imposing significant economic burdens on affected individuals (Carrera et al., 2018). Therefore, rapid detection of malignant transformations at the earliest stage of cancer is still vital for efficient treatments, suggesting that there is an urgent need for detection methods capable of identifying cancer-specific biomarkers that are not only highly sensitive and rapid, but also affordable and adaptable across diverse clinical settings.

This study combines computational fluid dynamics (CFD) analysis and experimental validation to evaluate the micromixing efficiency of a serpentine micromixer, called as TFU, and its capability to enhance nanoparticle–biomarker interactions under laminar flow conditions. To first confirm the fundamental functionality and reproducibility of the platform, the streptavidin–biotin system, widely recognized as a high-affinity and well-characterized interaction model (Chivers et al., 2011), was employed, using streptavidin-coated SPIONs exposed to increasing biotin concentrations. Building on this validation, the platform's performance under clinically relevant conditions was subsequently assessed using AFP, a diagnostic biomarker associated with hepatocellular carcinoma, by immobilizing AFP-specific monoclonal antibodies onto the SPION surface and examining capture behavior across varying AFP concentrations. Nanoparticle–ligand interactions were systematically characterized using DLS and NTA, revealing that the micromixer-enabled microfluidic system regulated binding events in a controlled and reproducible manner. Specifically, streptavidin–biotin experiments demonstrated preservation of nanoscale size distributions with limited aggregation following microfluidic processing, while AFP-binding studies exhibited stable and consistent nanoparticle size profiles over a broad concentration range (1–10^5 pg/mL), including low analyte levels. Collectively, these results indicate that micromixer integration effectively increases nanoparticle–biomarker encounter probability under laminar flow, providing a robust and scalable foundation for point-of-care diagnostic platforms targeting early-stage disease detection.

2. Materials and methods

2.1. Materials

A 4-inch n-type silicon wafer with a <100> crystallographic orientation (University Wafer) was used as the substrate for fabricating the SU-8 mold (Supporting **Information, S1**), employing SU-8 3050 negative photoresist (Microresist Technology). For fluidic interfacing, PTFE tubing with an outer diameter of 1/16″ and standard connection elements (Darwin Microfluidics) were utilized. Upon completion of the bonding process, inlet and outlet ports were carefully opened, and the tubing connections were integrated into microfluidic chips to ensure reliable fluid handling. For nanoparticles, Iron (II) chloride and iron (III) chloride were obtained from Merck (purity level: 99%, Darmstadt, Germany). Poly(acrylic acid) (PAA) (MW 5100 Da) was purchased from Sigma (MO, USA). Vivaspin 20 centrifugal filters were acquired from Sartorius (Göttingen, Germany). Streptavidin was purchased from New England Biolabs (MA, USA). AFP protein was purchased from MyBioSource (CA, USA), and monoclonal AFP antibody was sourced from R&D Systems (MN, USA). Ethyl-3-(3-dimethylaminopropoyl) carbodiimide (EDC) was provided by Sigma-Aldrich (USA), and N-hydroxysulfosuccinimide (sulfo-NHS) was obtained from Tokyo Chemical Industry (Japan). Ultra-pure water (18.2 MΩ) used for the experiments was supplied by Rephile Bioscience and Technology (Shanghai, China).

2.2. Synthesis of polyacrylic acid-coated SPIONs

Poly (acrylic acid) coated superparamagnetic iron oxide nanoparticles were synthesized (Fig. 1.) by a co-precipitation method from iron salts (Fe_3^+: Fe_2^+ = 2:1) previously optimized in the previous study of the research group (Bilici et al., 2018, 2020). Briefly, iron salts and polyacrylic acid (1.2 g) were mixed in deoxygenated water and dissolved at 85 °C for 20 min. Then, NH4OH (9.26 mL of 4.5 M) was added to the solution, and the reaction continued at the same temperature for an additional hour. Once complete, the solution was allowed to cool to room temperature and then placed on a magnet overnight to remove any precipitated material. The synthesized nanoparticles were washed with deionized water using 5 kDa ultrafiltration tubes and stored at room temperature.

2.3. Conjugation of streptavidin and AFP protein to PAA-SPIONs

Streptavidin and AFP protein were conjugated to polyacrylic acid-coated superparamagnetic iron oxide nanoparticles with an amidation reaction utilizing carbodiimide chemistry, as displayed in Fig. 2. 5% of the carboxylic acid groups on the surface of the nanoparticles were targeted for streptavidin conjugation. SPIONs were first transferred into a 0.1 M MES buffer (pH = 6), and carboxylic acid groups were activated with EDC and sulfo-NHS. The reaction was performed at room temperature for 30 min. Then the sample was washed with PBS buffer (pH = 7.4) to remove unreacted EDC and sulfo-NHS via ultracentrifugation. The desired amount of streptavidin and AFP protein was added to the sample solution and reacted at room temperature overnight. The next day, the pH of the sample solution was adjusted to 8.5, and again washed with PBS buffer. The washed solution was collected for Bradford analysis. Bovine serum albumin was dissolved in PBS at various concentrations to create a standard. Coomassie blue was added to both the standards and the collected washed samples, and the absorbance at 595 nm was recorded for each one. The concentrations and corresponding conjugation efficiency were calculated based on the standards. The final conjugated particles (Strep-PAA-SPION and AFP-PAA-SPION) were stored in the dark at 4 °C.

2.4. Characterization of nanoparticles

The iron content of the SPIONs was quantified using an Agilent 7700X inductively coupled plasma mass spectrometer (ICP-MS). The samples underwent thorough etching with 65% nitric acid and 96% sulfuric acid. The absorption spectrum of the SPIONs was analyzed with a Shimadzu UV-VIS-NIR spectrophotometer. Hydrodynamic sizes and zeta potentials were measured using a Malvern Zetasizer Nano ZS (Supporting **Information, S2**).

2.5. Numerical simulation

Under the assumption of incompressible and steady flow, the continuity equation, also known as mass conservation, can be applied in its simplified form (Batchelor, 2000; Stone et al., 2004):

$$\nabla.\vec{u} = 0 \tag{1}$$

Here, $\vec{u}$ represents the velocity vector of the fluid. Accordingly, mixing between two liquids is governed entirely by diffusion, convection, and geometric effects (Nguyen, 2011).

Navier–Stokes equations, which are based on the momentum equations, should be also solved (Schneiderbauer and Krieger, 2013). In microfluidic systems, fluids typically flow at low Reynolds numbers which suggests laminar flow conditions (Amini et al., 2014). Here, the transport characteristics and solute distribution within the proposed micromixer geometries were resolved through numerical modeling in COMSOL Multiphysics 6.3, employing finite-element method (FEM). Navier–Stokes, and convection–diffusion equations are expressed as:

$$\frac{\partial V}{\partial t} + \rho(V.\nabla)V = -\nabla P + \mu\nabla^2 V \tag{2}$$

$$\frac{\partial C}{\partial t} + (V.\nabla)C = \mathrm{D}\nabla^2 C \tag{3}$$

where V indicates the velocity field, P is the pressure, C is the concentration of a solute and D is the diffusion coefficient.

The non-dimensional Reynolds number is defined as:

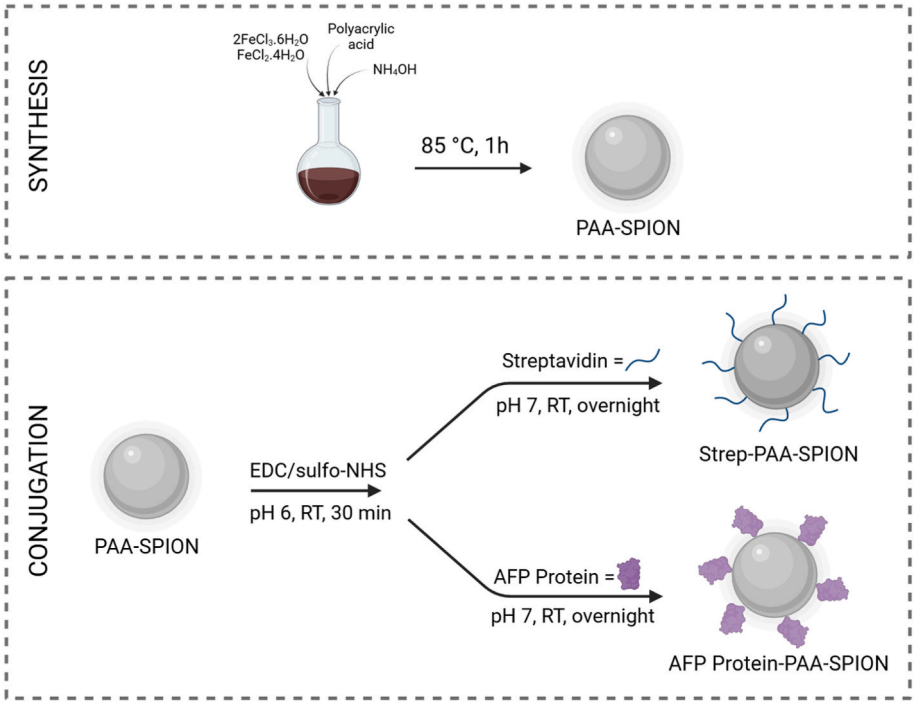

Fig. 1. Visual explanation of nanoparticle synthesis, surface chemistry and conjugation, protein immobilization used in the present study.

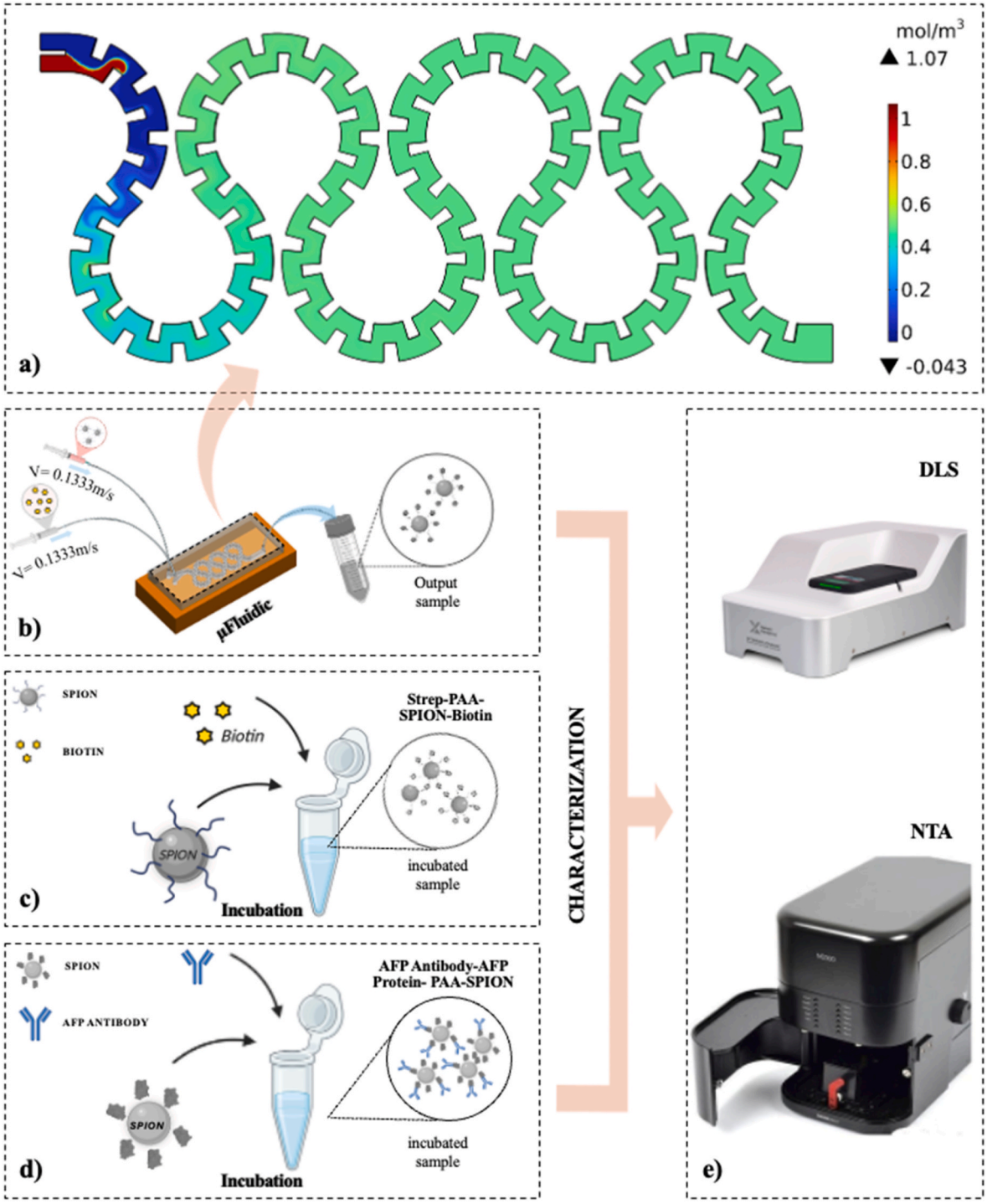

Fig. 2. Experimental setup with (a) concentration profile of mixing fluids showing the maximum mixing performance at $R_e = 50$ and with $0.5 mol/\ m^3$ molarity, in a micromixer with quasi-rectangular baffle shapes reproduced from reference (Ahmadi et al., 2021) with permission, (b) streptavidin-immobilized SPIONs and biotin were infused through the micromixer and, in parallel, (c) streptavidin-immobilized SPIONs and biotin were incubated in a controlled container for the same duration as the micromixing process. (d) A similar incubation procedure was performed for AFP antibody–AFP protein interactions with PAA-coated SPIONs. (e) The resulting samples were then collected and characterized using DLS and NTA.

$$R_e = \frac{\rho U D_h}{\mu} \tag{3}$$

Here, ρ is the fluid density, U is the average velocity, μ is the viscosity, and $D_h = \frac{4A}{P}$ with cross the cross-sectional area (A) and wetted perimeter (P) of the microchannel. The design includes curved microchannel structures with radius of curvature (R) (Supporting **Information, S3. Design Parameters**), secondary circulation develops, which can be quantified through the Dean number defined as:

$$D_e = R_e \sqrt{\frac{D_h}{2R_c}} \tag{4}$$

The fluids were considered as Newtonian and incompressible, and a steady-state assumption was made. At the inlet, a uniform velocity profile was imposed, while the outlet was constrained to zero static

pressure. The wall satisfied no-slip conditions. Two fluid streams were introduced with normalized concentrations of 0 and 1. The perfect mixing was therefore defined at a molar concentration of 0.5. The interdiffusion coefficient of the two streams was set to $3.6\,x\,10^{-10} m^2/\,s$. The geometry (Supporting **Information, S3**) is a single manifold solid with extensive curved features (465 faces; 462 circular features; 231 cylindrical surfaces; 234 planes) and rich topology (15,783 entities). Discretization used a user-controlled, fluid-dynamics–oriented unstructured triangular mesh with custom sizing (max/min $2.5 \times 10^{-5}/2.9 \times 10^{-6}$ m; growth 1.1), curvature and narrow-region controls (0.4/0.9), corner refinement at tips and constrictions, and wall boundary layers to resolve near-wall gradients, yielding a numerically robust grid for coupled laminar-flow and species-transport analyses. The final solve involved 3,264,391 degrees of freedom (plus 250,690 internal DoFs).

2.6. Post-processing

The fluorescent microscope images of the micromixer from top views were gathered by using ZEISS ZEN 3.10 software, and the images were extracted using ZEN BLUE 3.1 to determine mixing indices depending on fluorescent profiles that were obtained from the outlet of the micromixer. Then, the following expression was used to determine the mixing index (Fan et al., 2017; Ahmadi et al., 2021):

$$MI = 1 - \sqrt{\frac{1}{n}\sum_{i=1}^{n}\left(\frac{I_i - \bar{I}}{\bar{I}}\right)^2} \tag{5}$$

Here, MI represents the mixing index, n indicates the number of pixels in profile line, $\bar{I}$ refers to mean fluorescent intensity of all pixels in the profile line, and I_i stands for the fluorescence intensity of the ith pixel.

The governing equations and associated dimensionless numbers establish a mathematical foundation for the design and evaluation of micromixers. This framework not only enables accurate numerical analysis but also provides a reliable basis for modeling and experimental validation.

3. Experimental design

The experiments were primarily conducted using sample infusing through the micromixer and conventional incubation methods (Fig. 2). For platform validation streptavidin-conjugated SPION suspensions were injected through one inlet of the micromixer with $R_e = 20$, and the biotin analyte solution was infused to the other inlet. Following the micromixing process, the mixed samples were collected from the outlet and subsequently analyzed by DLS and NTA. For the streptavidin-conjugated SPIONs–biotin binding experiments, biotin solutions were prepared in PBS. In the second stage, AFP-protein-conjugated SPIONs were processed under the same micromixing and incubation conditions. Nanoparticle size distributions evaluated by DLS and NTA.

Experiments were performed at room temperature. Streptavidin-coated SPIONs were reacted with biotin under two conditions: microfluidic micromixing with an experimental duration of ~10 min, and static incubation in microcentrifuge tubes for the same duration. Concentrations, total volume, and buffer composition were kept identical during the tests.

4. Results and discussion

4.1. Numerical and experimental analysis of micromixer

Building on the findings of our previous investigation on micromixing with serpentine microchannels having baffle elements of different properties, we identified micromixer model M3 as achieving the fast and efficient mixing ratio in a short mixing length (Ahmadi et al., 2021). This design has a robust and highly efficient mixing performance across broad ranges of flow rates. The microfluidic chip features a quasi-rectangular baffle design, with a baffle width of 150 μm, a baffle angle of 8.75°, and a baffle spacing of 26.25°. Geometric parameters were used to calculate the cross-sectional area of the channel, defined by a microchannel thickness (t) of 100 μm and a width (w) of 300 μm. An inlet flow average velocity of approximately 0.133 m/s leads to a Reynolds number (Re) of 20 and a Dean number (De) of 7.75, resulting in a mixing efficiency of ~98%.

In order to obtain a more comprehensive understanding of the inertial effects governing the mixing mechanism, we further investigated the flow behavior within the microfluidic chip through an analysis of molar concentration profiles and velocity magnitudes. As shown by the molar concentration profiles and velocity magnitudes (Fig. 3), the presence of baffle structures enhances the mixing efficiency by promoting stronger chaotic advection (Ahmadi et al., 2021). At low Reynolds numbers (~1), transport is governed primarily by molecular diffusion, which leads to the persistence of sharp concentration gradients and the formation of low-velocity regions within the baffle geometries. Under these conditions, micromixing is inefficient, as the interface between fluid streams remains largely undisturbed. When the Reynolds number increases to intermediate values ($R_e = 5 - 10$. The combined influence of the channel curvature and geometric corrugation generates secondary Dean vortices (Ahmadi et al., 2021). The vortices continuously stretch and fold concentration profiles, initiating chaotic advection and significantly improving local mixing performance (El Hani et al., 2025; Habchi et al., 2013). At higher Reynolds numbers (20–30), the secondary vortices intensify and occupy the entire cross-section, periodically redistributing fluid between the inner and outer channel walls. This redistribution of species produces a far more homogeneous concentration field along the channel length, representing a regime, where the mixing efficiency is maximized (Saffar et al., 2023). Beyond this range (Re ≈ 40–50), advection becomes dominant, driving near-complete homogenization (Jiang et al., 2004). However, the corresponding reduction in the residence time and increase in the hydraulic resistance impose practical limitations, particularly for processes that require longer reaction times.

During the experiments, top-view fluorescence images were acquired using the tile-scan mode of the fluorescent microscope and reconstructed by stitching the sectional images (Fig. 4). Subsequently, image processing of the reconstructed frames generated concentration intensity profiles, from which the mixing index (MI) was calculated for each flow condition. According to the results, the micromixer achieves a mixing index of 0.98 at Re = 20 after starting at 0.62 at Re = 1 (Ahmadi et al., 2021), and extended residence times allow diffusion-driven mixing at low Reynolds numbers, while higher velocities show chaotic advection, enhancing the mixing performance, Fig. 4-b. The quasi-rectangular baffles in this design promote high vortex formation and flow disturbances, boosting mass transfer and enabling high efficiency even at low Re. Beyond Re = 20, the mixing performance stabilizes between 0.97 and 0.98, showing that relatively low flow rates are sufficient for optimal mixing.

Overall, the transition from diffusion-limited to advection-dominated transport reflects the strong interplay between the serpentine curvature and corrugated wall structures. At low Reynolds numbers, mixing is dictated by slow molecular diffusion, while increasing flow rates induce vortex-driven advection that progressively enhances homogenization. The intermediate regime (Re ≈ 20–30) offers a favorable balance, delivering a high micromixing efficiency without incurring excessive energy penalties, and can therefore be considered the optimal operating condition for most applications.

4.2. Nanoparticle characteristics

The integration of nanoparticles with a micromixing platform provides distinct advantages for biomarker capture, as nanoparticles provide a high surface-to-volume ratio that enables efficient analyte

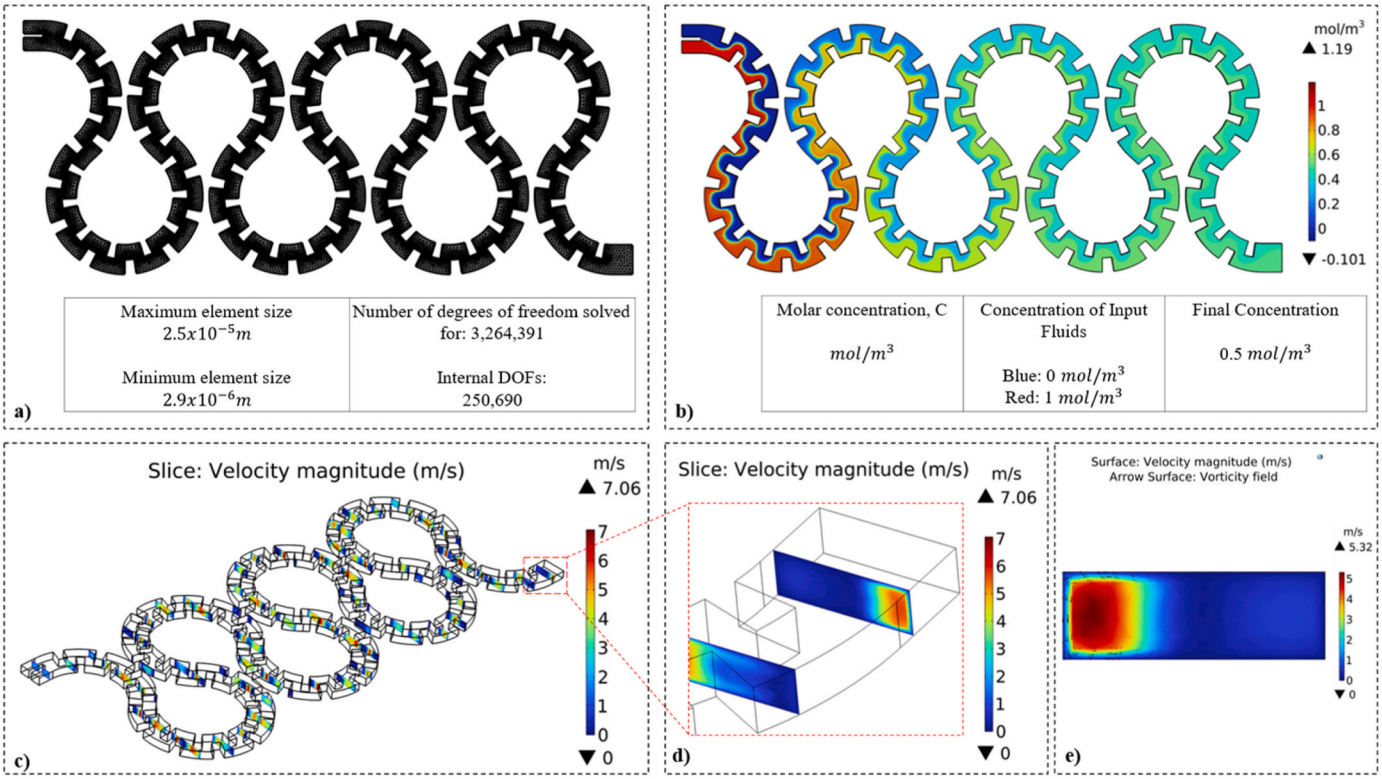

Fig. 3. Simulation properties of micromixing. (a) Meshing used a user-controlled, fluid-dynamics–calibrated sequence. An unstructured free tetrahedral grid was generated with custom sizing (max 2.5×10^{-5} *m*; min 2.9×10^{-6} *m*; growth 1.1; curvature 0.4; narrow-region 0.9). Local control via a second size node and corner refinement on selected boundaries sharpened baffle sections, while boundary-layer elements on all walls resolved near-wall velocity and concentration gradients. The resulting mesh is well graded, coarser in the bulk and deliberately dense around baffles, corners, and constrictions, supporting accurate, stable laminar-flow and species-transport solutions. (b) Steady-state molar concentration C (mol/m^3) in the serpentine micromixer. Two inlet streams, blue with C = 0, and red with C = 1 mol/m^3 are split, folded, and recombined along successive loops, enhancing transverse mixing; the outlet approaches a uniform C ~0.5 mol/m^3. The color bar spans 0-1 mol/m^3. (c) Velocity magnitudes (m/s) in different sections in micromixer, (d) Orthogonal plane through micromixer's end showing contraction-induced jetting: velocity peaks near the throat (up to ~7 m/s by the scale), with steep shear layers that relax downstream. This highlights where mixing is driven by strong local acceleration due to the baffle section. (e) An end plane map reveals a high-speed entry region (~5.3 m/s by the scale) that generates counter-rotating vortices; the vortical intensity decays downstream as the profile becomes more uniform. The vorticity field indicates secondary flows that enhance transverse transport. (For interpretation of the references to color in this figure legend, the reader is referred to the Web version of this article.)

binding (Zhang et al., 2019). In parallel, micromixing enhances nanoparticle analyte interaction rates under laminar flow conditions, improving efficiency even at low analyte concentrations. These enhanced interactions can lead to measurable changes in nanoparticle hydrodynamic behavior and size distributions that reflect changed binding stage and colloidal organization (Li et al., 2022).

Colloidally stable, aqueous PAA-SPIONs were synthesized in small hydrodynamic sizes (number-based hydrodynamic size of 13.2 nm) with a strong negative zeta potential (−55.3 mV) (Supporting **Information, S2**). The streptavidin was covalently attached to SPION via EDC/NHS chemistry. According to Bradford assay results, the conjugation efficiency was calculated as 98%. The observed increase in the hydrodynamic size, from 154.2 to 184.3 nm based on the intensity average, and a decrease in the zeta potential to −35.0 mV indicate successful protein attachment. AFP-specific antibodies were conjugated using the same chemistry. An increase in hydrodynamic size from 12.3 nm to 296.5 nm based on intensity average and a decrease in zeta potential to −18.2 mV were observed.

4.3. Streptavidin conjugated SPIONs and biotin interactions

During the experiments, the DLS and NTA analysis techniques were used to comprehensively evaluate the size distributions of nanoparticles. The DLS reveals general changes in the hydrodynamic size and possible aggregation trends (Rodriguez-Loya et al., 2024), and the NTA allows for a detailed evaluation of the size distribution and concentration of individual particles (Filipe et al., 2010). Through these complementary analyses, changes in hydrodynamic size occurring during the interaction of streptavidin-conjugated SPIONs with biotin under both microfluidic treatment and conventional incubation conditions were examined. To evaluate the performance of the micromixer-based microfluidic platform, streptavidin-conjugated SPIONs were initially used with varying concentrations of biotin. Streptavidin-biotin interactions were used as a model in the system experiment because they are described in the literature as high-affinity interactions (Ozawa et al., 2017). The outputs obtained after microfluidic treatment and conventional incubation were compared by analyzing the nanoparticle size distribution. Thus, the effect of controlled mixing on binding dynamics was investigated. NTA and DLS analyses showed that in the microfluidic platform, as biotin concentration increased, the dominant size population of nanoparticles was maintained at the nanoscale, and there was no significant shift towards larger size populations. This indicates that micromixing integration prevented uncontrolled aggregation formation. In contrast, samples prepared using the incubation method showed greater size distribution, especially at high biotin concentrations, and increased heterogeneity of the system.

In the experiments, biotin concentration was adjusted to range from 0 to 12.22 ng/mL, with values of 0, 0.24, 1.22, 2.44, 4.89, 9.77, and 12.22 ng/mL used, respectively. The interaction of streptavidin-conjugated SPIONs with biotin was evaluated using number-based

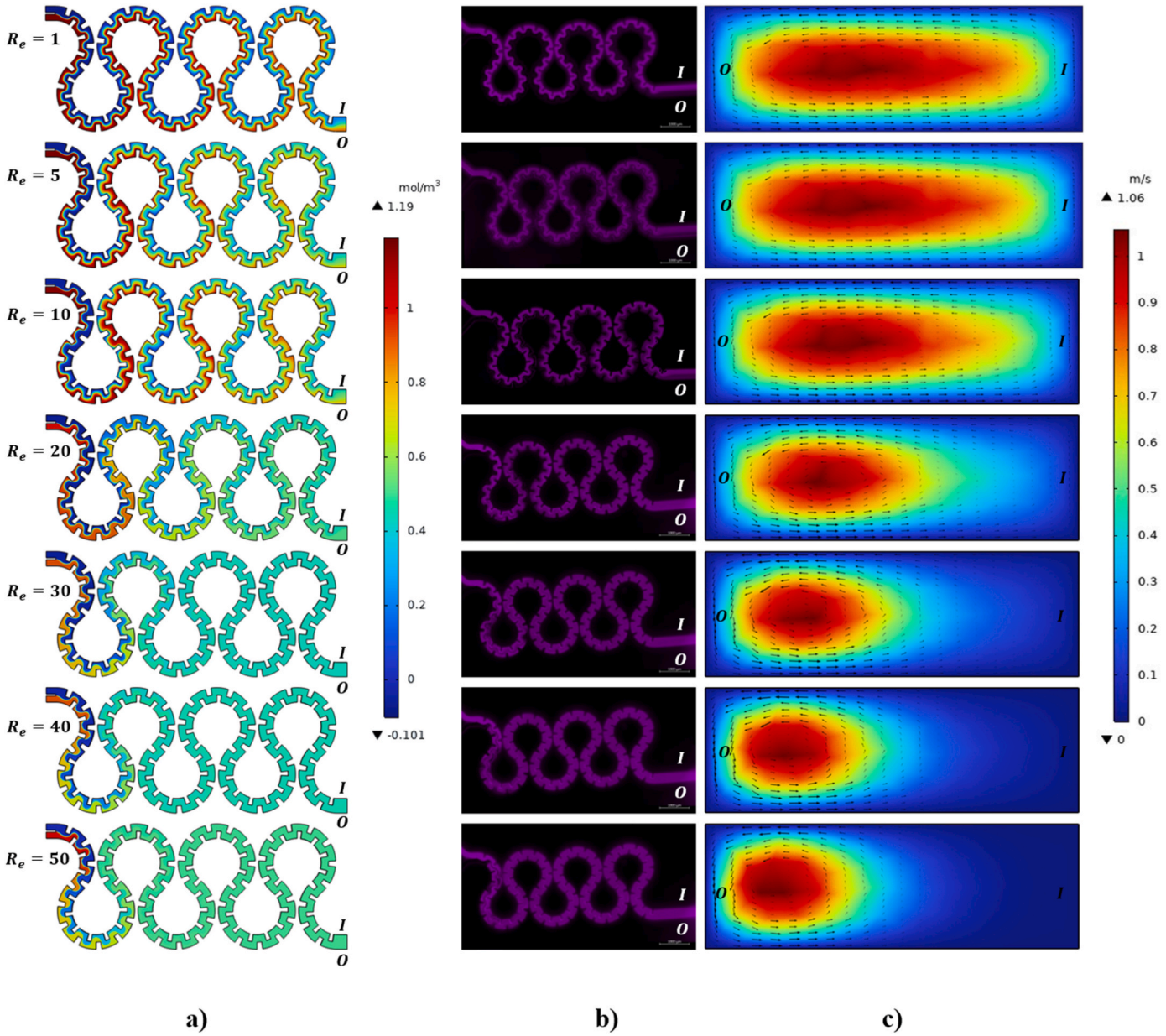

Fig. 4. Flow characteristics of micromixer with (a) concentration profiles in mol/m^3 with varying Reynolds numbers $R_e = 1, 5, 10, 20, 30, 40, 50$, (b) experimental results of micromixing process in different R_e obtained by fluorescent microscopy reproduced from reference (Ahmadi et al., 2021) with permission, and (c) velocity magnitudes (m/s) of vorticity fields depending on varying Reynolds number. Here, **I** represent the inner wall, and **O** corresponds to the outer wall of the outlet of the microchannel.

DLS analysis under a microfluidic system (Fig. 5). At low biotin concentrations (0.1 ng/mL $\leq$), the nanoparticles exhibited hydrodynamic sizes around ~20 nm, while a significant increase in the average hydrodynamic diameter (up to 30 nm) was observed with increasing concentration. At higher concentrations (>1 ng/mL), the decrease in sizes suggests that the additional biotin provides a limited contribution to nanoparticle size after the binding sites approach saturation (Fig. 5-b). The observation of similar trends in three independent experiments (Fig. 5-b) indicates that the results obtained under microfluidic treatment are reproducible and controlled. In contrast, experiments conducted under conventional incubation conditions showed that the average hydrodynamic sizes exhibited a more irregular variation depending on the biotin concentration (Fig. 5-c). The increases and decreases observed at different concentration points indicate that nanoparticle-biotin interactions occur less controllably in the incubation method. Furthermore, the higher variation between independent experiments compared to microfluidic conditions suggests that random encounters and local concentration differences may occur during incubation. Overall, the comparative DLS and NTA results reveal that the microfluidic system can direct streptavidin-biotin interactions in a more homogeneous and reproducible.

4.4. AFP specific protein conjugated SPIONs and AFP protein interactions

To evaluate the performance of the microfluidic platform, SPIONs functionalized with AFP-specific antibodies were used. Experiments on AFP binding were performed under incubation and microfluidic treatment conditions at a wide concentration range (1–100,000 pg/mL), and nanoparticle size changes were analyzed using DLS and NTA techniques (Fig. 6).

Number-based DLS results show significant but irregular changes in average hydrodynamic diameter values depending on AFP

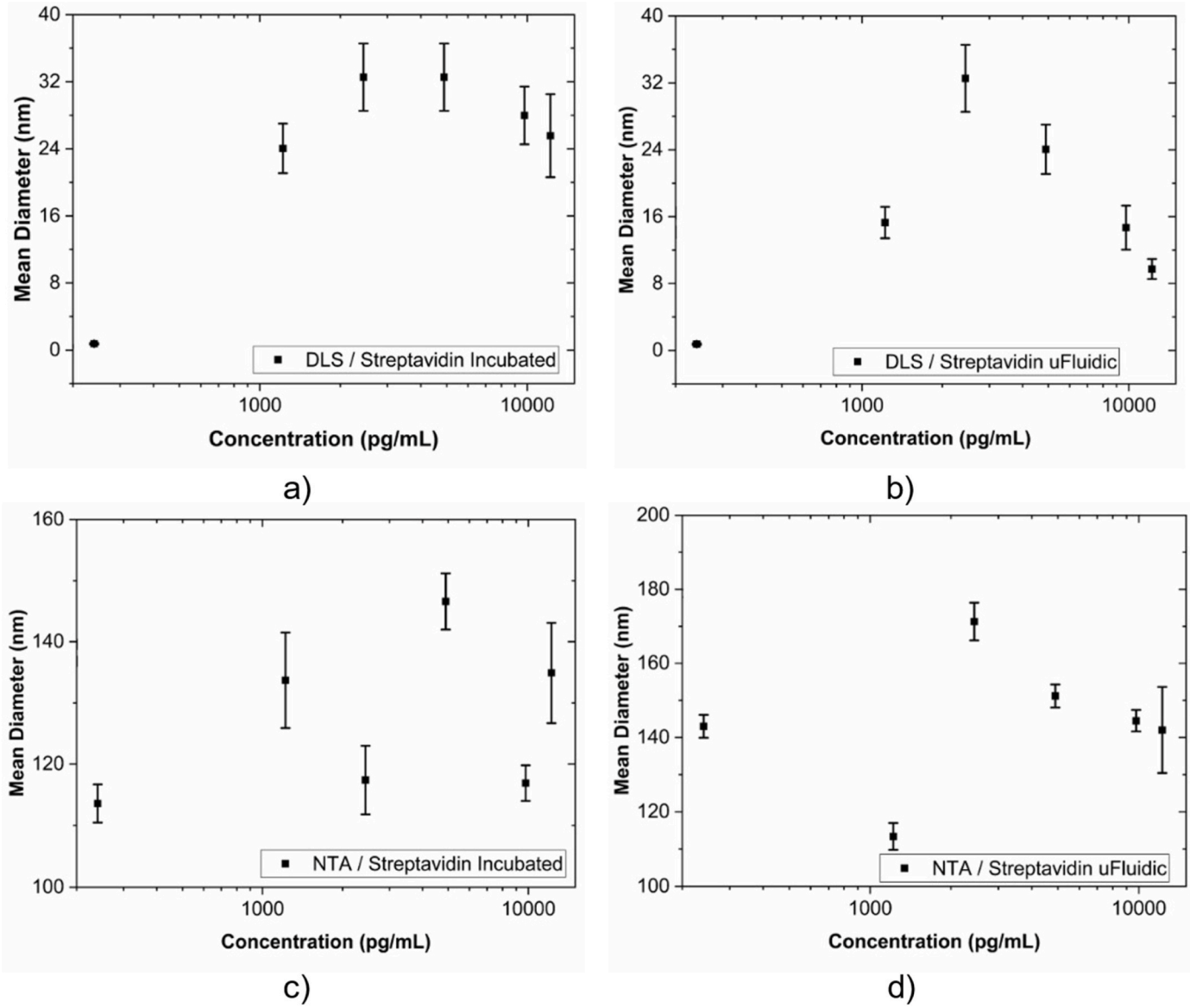

Fig. 5. Comparison of mean hydrodynamic diameters of streptavidin-conjugated SPIONs at different biotin concentrations (0–12.22 ng/mL) under incubation and microfluidic processing conditions. (a) Mean hydrodynamic diameter values measured by number-based DLS under incubation conditions. (b) Number-based DLS results for samples processed in a microfluidic system. (c) Mean nanoparticle sizes obtained by NTA under incubation conditions. (d) Mean nanoparticle sizes measured by NTA after microfluidic processing. Data show mean values from three independent experiments, and error bars represent the standard deviation (mean ± SD, n = 3). Under microfluidic processing, both DLS and NTA results show a more regular and reproducible size behavior depending on the biotin concentration.

concentration under incubation conditions (Fig. 6-a). In particular, the abrupt increases and decreases observed at different concentration points indicate that the binding process occurs more heterogeneously and less controlled under the incubation method. In contrast, DLS measurements in microfluidic treated samples showed a more consistent size change trend throughout the AFP concentration (Fig. 6-b). This suggests that microfluidic mixing directs nanoparticle–AFP interactions in a more controlled manner. NTA results revealed that the dominant nanoparticle population remained at the nanoscale under both treatment conditions but showed significant differences in distribution regularity between incubation and microfluidic treatment (Fig. 6 - c and d). Under incubation conditions, nanoparticle sizes varied over a wider range, and inter-experimental variation was higher. In contrast, NTA data obtained after microfluidic treatment exhibited a narrower size range and better reproducibility. These findings suggest that the microfluidic platform can facilitate nanoparticle–biomarker interactions in a more homogeneous and predictable environment during the capture of clinical biomarkers such as AFP.

Another aspect of the results of this study is that the size differences observed between DLS and NTA measurements across both streptavidin- and AFP-functionalized systems reflect fundamental differences in the underlying detection principles of the two techniques, rather than experimental inconsistency. DLS derives the hydrodynamic diameter from fluctuations in the scattered light intensity and is inherently intensity-weighted because light scattering scales strongly with the particle size. Even a small subpopulation of larger species or transient aggregates can dominate the signal and shift the apparent mean diameter. Importantly, this bias persists even in number-based DLS outputs, which are mathematically transformed from the intensity data and therefore remain sensitive to polydispersity (Filipe et al., 2010b; Farkas and Kramar, 2021). NTA, by contrast, tracks individual particles and calculates the size directly from their Brownian motion, yielding a true number-based distribution, in which each particle contributes equally regardless of the size (Kim et al., 2019). In protein-functionalized

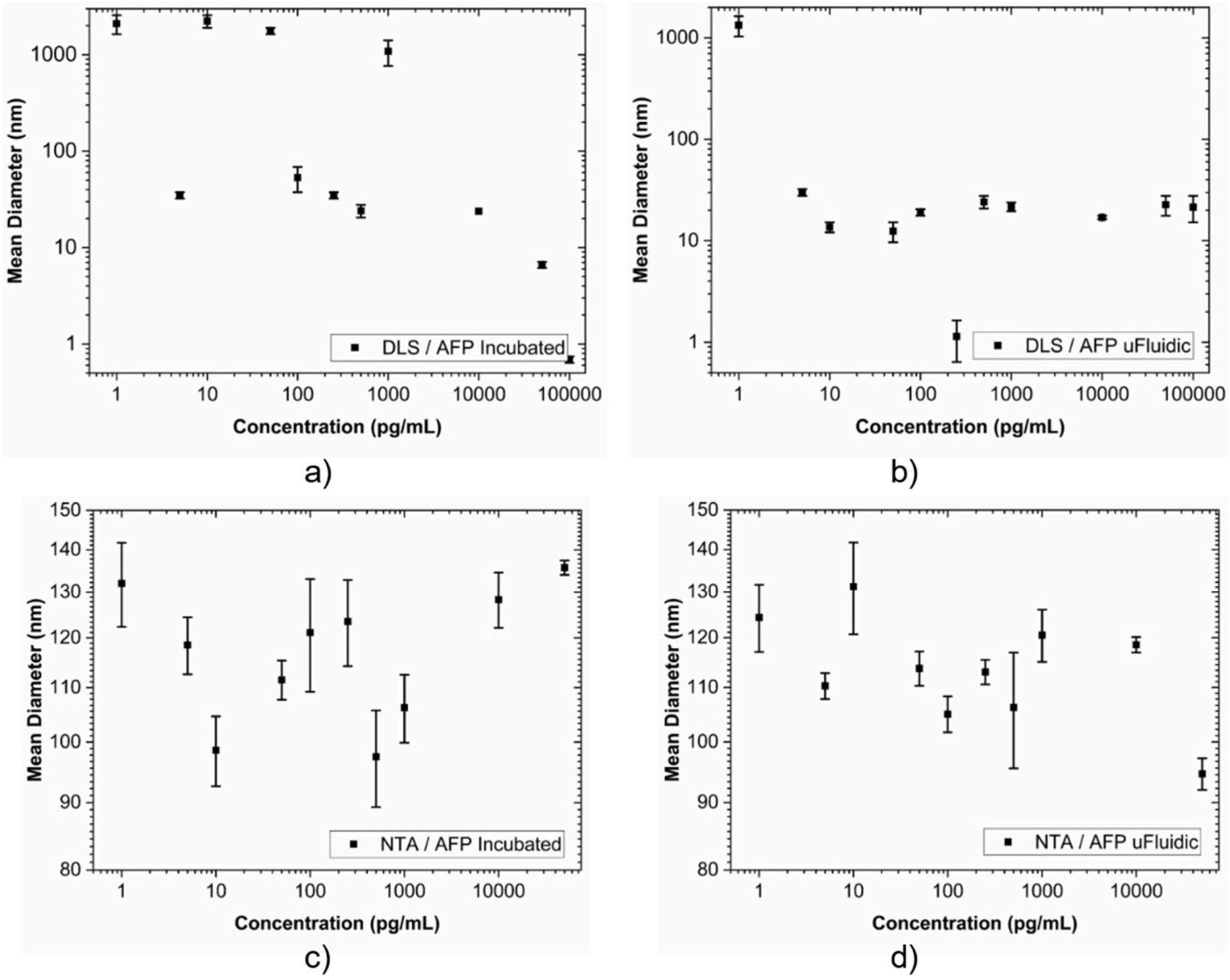

Fig. 6. Comparison of mean hydrodynamic diameters of SPIONs functionalized with AFP-specific antibodies under different AFP concentrations (1–100,000 pg/mL) and microfluidic processing conditions. (A) Mean hydrodynamic diameter values obtained by number-based DLS under incubation conditions. (B) Number-based DLS results for samples processed in a microfluidic system. (C) Mean nanoparticle sizes measured by NTA under incubation conditions. (D) Mean nanoparticle sizes obtained by NTA after microfluidic processing. Data show the mean values of three independent experiments, and error bars represent the standard deviation (mean ± SD, n = 3). Under microfluidic processing, both DLS and NTA measurements indicate a more regular and repeatable size distribution depending on the AFP concentration.

nanoparticle systems such as those studied here, DLS, therefore, captures an effective hydrodynamic diameter that integrates contributions from the nanoparticle core (Monopoli et al., 2012), protein corona, and surrounding solvation layer, while NTA more directly reflects the actual dominant particle population. This distinction becomes particularly apparent in the AFP datasets, where DLS reported substantially larger apparent diameters, especially in incubated samples at lower analyte concentrations, while NTA remained centered near approximately 100–135 nm, consistent with a polydisperse system, where the main nanoscale population is preserved but the DLS signal is disproportionately influenced by a minor fraction of larger species. The two methods, therefore, provide complementary rather than contradictory information, and together they offer valuable insight into both the bulk colloidal behavior and true particle size distribution of the system.

Importantly, this improvement in micromixing is expected to directly influence nanoparticle-protein interaction kinetics (Hu et al., 2019). By continuously redistributing nanoparticles and analyte molecules throughout the channel cross-section, the TFU micromixer reduces the local concentration gradients and increases the frequency of effective particle–analyte encounters (Agha et al., 2023). Compared with static incubation, this more homogeneous mixing environment is less prone to localized overconcentration, uneven surface binding, and uncontrolled interparticle aggregation. The dependence of the mean particle diameter on analyte concentration was not strictly monotonic in several datasets, and this behavior is most likely explained by a combination of analyte binding, restructuring of the adsorbed interfacial layer, and concentration-dependent interparticle interactions rather than binding-site occupancy alone (Vilanova et al., 2025). As the concentration increases toward surface saturation, bridging may be reduced, and the interfacial layer may become more uniform or compact, thereby decreasing the apparent diameter (Yu et al., 2020). The DLS and NTA results support this interpretation, as microfluidically processed samples generally maintained a more stable nanoscale population and exhibited less noticeable shifts toward larger particle sizes than incubated samples. Collectively, these findings indicate that the TFU platform improves not only the bulk mixing efficiency but also the uniformity and reproducibility of nanoparticle binding events.

5. Conclusion

Developing detection strategies based on the particle size distribution, particularly through passive microfluidic systems, can offer an energy-efficient and cost-effective alternative in the diagnosis of diseases. Herein, this study shows that particle size distribution–based detection, when combined with passive microfluidic preprocessing, can provide an energy-efficient and cost-effective approach for disease diagnostics. A stepwise comparison between microfluidic mixing and conventional incubation revealed that micromixing improves the uniformity of binding kinetics between streptavidin-immobilized SPIONs and target molecules over concentrations of 0, 1, 5, 10, 20, 40, and 50 nM. While the micromixer chip is not intended to operate as a standalone detection platform, it functions effectively as a TFU that standardizes the particle–particle interactions and improves the reliability of downstream nanoparticle dimensional analysis.

At the optimized operating condition of Re ≈ 20, the system achieved a mixing index of ~0.98, indicating near-complete homogenization while preserving sufficient residence time for nanoparticle–analyte binding. Under these hydrodynamic conditions, ~1 nM concentration increments produced measurable and reproducible hydrodynamic size shifts, with lower standard deviation and narrower NTA size distributions across replicates (n = 3) than those obtained by conventional incubation. These results confirm that controlled advection-driven mixing reduces the variability and enables more linear and quantitative calibration of binding-induced size changes.

The platform is also not limited to size-based readout. Although size shifts in the range of about 10–30 nm were resolved depending on surface functionalization, the same controlled micromixing strategy may support other outputs, including plasmonic or colorimetric intensity changes, magnetic relaxation in SPION-based systems, fluorescence modulation, and improved particle capture before downstream molecular assays such as PCR. In PCR-based diagnostic workflows, target capture or enrichment steps are performed under conventional incubation conditions (Chen et al., 2020) which may result in heterogeneous binding and capture efficiency variability. Thus, micromixing-assisted processing can improve the capture uniformity and also provide more consistent nanoparticle-target interaction, which potentially reduces the variety in PCR pretreatment steps and improves the reproducibility of molecular detection workflows. From an engineering perspective, the operation at Re ≈ 20 offers an effective compromise between high mixing efficiency, practical flow rate, and acceptable hydraulic resistance, enabling preprocessing within seconds rather than the tens of minutes or hours typically required for conventional incubation (Bazaz et al., 2018; Materón et al., 2021; Ha and Kim, 2022).

Overall, the platform should be viewed as a modular interaction-control unit that delivers a high mixing efficiency (~98%) (Ahmadi et al., 2021), reproducible nanometer-scale signal shifts, and improved inter-experimental consistency. Its compatibility with optical, magnetic, molecular, and droplet-based microfluidic systems makes it a promising building block for point-of-care diagnostics, multiplexed biosensing, high-throughput screening, and nanomedicine applications such as formulation optimization, aggregation studies, and stability profiling under defined shear and residence-time conditions.

CRediT authorship contribution statement

İsmail Bütün: Writing – review & editing, Writing – original draft, Validation, Project administration, Methodology, Investigation, Data curation, Conceptualization. **Melis Hazal Porsuk:** Writing – review & editing, Writing – original draft, Validation, Methodology, Investigation, Conceptualization. **Mine Demir Khan:** Writing – review & editing, Writing – original draft, Validation, Investigation, Formal analysis. **İrem Acar:** Writing – review & editing, Writing – original draft, Validation, Investigation. **Sibel Çetinel:** Writing – review & editing, Writing – original draft, Validation, Supervision, Resources, Project administration, Methodology, Conceptualization. **Özlem Kutlu:** Writing – review & editing, Writing – original draft, Supervision, Resources, Project administration, Methodology, Formal analysis, Conceptualization. **Havva Funda Y. Acar:** Writing – review & editing, Writing – original draft, Validation, Supervision, Resources, Project administration, Methodology, Formal analysis, Conceptualization. **Ali Koşar:** Writing – review & editing, Writing – original draft, Supervision, Resources, Project administration, Methodology, Investigation, Funding acquisition, Conceptualization.

Informed consent statement

Not applicable.

Institutional review board statement

Not applicable.

Declaration of generative AI and AI-assisted technologies in the writing process

During the preparation of this manuscript, the authors used ChatGPT (version 5.2) exclusively for language refinement and stylistic improvements. The tool was not used to generate scientific content, data, or interpretations. All outputs were critically reviewed and edited by the authors, who take full responsibility for the content of the publication.

Funding

This research was funded by TÜBİTAK (The Scientific and Technological Research Council of Türkiye) 1004 NANOSIS Programme, Grant Number 20A6012, and by Merck GmbH scholarship program (Türkiye). The funders had no role in the study design, data collection, or analysis, the decision to publish, or the preparation of this manuscript.

Declaration of competing interest

The authors declare that they have no known competing financial interests or personal relationships that could have appeared to influence the work reported in this paper.

Appendix A. Supplementary data

Supplementary data to this article can be found online at https://doi.org/10.1016/j.biosx.2026.100783.

Data availability

Data will be made available on request.

References

Åberg, C., Piattelli, V., Montizaan, D., Salvati, A., 2021. Nanoscale 13, 17530–17546. https://doi.org/10.1039/D1NR04690J.
Adedokun, G., Alipanah, M., Fan, Z.H., 2024. Lab Chip 24, 3626–3650. https://doi.org/10.1039/D3LC00943B.
Agha, A., Waheed, W., Stiharu, I., Nerguizian, V., Destgeer, G., Abu-Nada, E., Alazzam, A., 2023. Discov. Nano 18, 18. https://doi.org/10.1186/s11671-023-03792-x.
Ahmadi, V.E., Butun, I., Altay, R., Bazaz, S.R., Alijani, H., Celik, S., Warkiani, M.E., Koşar, A., 2021. Chem. Eng. Res. Des. 168, 490–498. https://doi.org/10.1016/j.cherd.2021.02.028.
Amini, H., Lee, W., Di Carlo, D., 2014. Lab Chip 14, 2739–2761.
Ammar, H., Zoghbi, B.E., Faraj, J., Khaled, M., 2025. Chem. Eng. Process. Process Intensif. 208, 110098. https://doi.org/10.1016/j.cep.2024.110098.
Ardila, C.M., Jiménez-Arbeláez, G.A., Vivares-Builes, A.M., 2024. Dent. J. 12. https://doi.org/10.3390/dj12010005.
Atencia, J., Beebe, D.J., 2005. Nature 437, 648–655. https://doi.org/10.1038/nature04163.

Ayuso, J.M., Virumbrales-Muñoz, M., Lang, J.M., Beebe, D.J., 2022. Nat. Commun. 13, 3086. https://doi.org/10.1038/s41467-022-30384-7.
Batchelor, G.K., 2000. Cambridge University Press, Cambridge. https://doi.org/10.1017/CBO9780511800955.
Bayareh, M., Ashani, M.N., Usefian, A., 2020. Chem. Eng. Process. Process Intensif. 147, 107771. https://doi.org/10.1016/j.cep.2019.107771.
Bazaz, S.R., Mehrizi, A.A., Ghorbani, S., Vasilescu, S., Asadnia, M., Warkiani, M.E., 2018. RSC Adv. 8, 33103–33120. https://doi.org/10.1039/C8RA05763J.
Bi, W.L., Hosny, A., Schabath, M.B., Giger, M.L., Birkbak, N.J., Mehrtash, A., Allison, T., Arnaout, O., Abbosh, C., Dunn, I.F., Mak, R.H., Tamimi, R.M., Tempany, C.M., Swanton, C., Hoffmann, U., Schwartz, L.H., Gillies, R.J., Huang, R.Y., Aerts, H.J.W. L., 2019. CA Cancer J. Clin. 69, 127–157. https://doi.org/10.3322/caac.21552.
Bilici, K., Muti, A., Demir Duman, F., Sennaroğlu, A., Yağcı Acar, H., 2018. Photochem. Photobiol. Sci. 17, 1787–1793. https://doi.org/10.1039/c8pp00203g.
Bilici, K., Atac, N., Muti, A., Baylam, I., Dogan, O., Sennaroglu, A., Can, F., Yagci Acar, H., 2020. Biomater. Sci. 8, 4616–4625. https://doi.org/10.1039/D0BM00821D.
Boussommier-Calleja, A., Li, R., Chen, M.B., Wong, S.C., Kamm, R.D., 2016. Trends Cancer 2, 6–19. https://doi.org/10.1016/j.trecan.2015.12.003.
Capretto, L., Cheng, W., Hill, M., Zhang, X., 2011. Microfluidics: Technologies and Applications. Springer, Berlin Heidelberg, Berlin, Heidelberg, pp. 27–68. https://doi.org/10.1007/128_2011_150.
Carrera, P.M., Kantarjian, H.M., Blinder, V.S., 2018. CA Cancer J. Clin. 68, 153–165. https://doi.org/10.3322/caac.21443.
Chen, Y., Liu, Y., Shi, Y., Ping, J., Wu, J., Chen, H., 2020. TrAC, Trends Anal. Chem. 127, 115912. https://doi.org/10.1016/j.trac.2020.115912.
Chivers, C.E., Koner, A.L., Lowe, E.D., Howarth, M., 2011. Biochem. J. 435, 55–63. https://doi.org/10.1042/BJ20101593.
El Hani, N., Lacassagne, T., Hamidouche, S., Bahrani, S.A., 2025. Rev. Sci. Instrum. 96, 061501. https://doi.org/10.1063/5.0254063.
Fan, L.-L., Zhu, X.-L., Zhao, H., Zhe, J., Zhao, L., 2017. Microfluid. Nanofluidics 21, 36.
Farkas, N., Kramar, J.A., 2021. J. Nanoparticle Res. 23, 120. https://doi.org/10.1007/s11051-021-05220-6.
Filipe, V., Hawe, A., Jiskoot, W., 2010. Pharm. Res. 27, 796–810. https://doi.org/10.1007/s11095-010-0073-2.
Fitzgerald, R.C., Antoniou, A.C., Fruk, L., Rosenfeld, N., 2022. Nat. Med. 28, 666–677. https://doi.org/10.1038/s41591-022-01746-x.
Gharib, G., Bütün, İ., Muganlı, Z., Kozalak, G., Namlı, İ., Sarraf, S.S., Ahmadi, V.E., Toyran, E., van Wijnen, A.J., Koşar, A., 2022. Biosensors 12. https://doi.org/10.3390/bios12111023.
Gimondi, S., Ferreira, H., Reis, R.L., Neves, N.M., 2023. ACS Nano 17, 14205–14228. https://doi.org/10.1021/acsnano.3c01117.
Ha, Y., Kim, I., 2022. Biochip J. 16, 351–365. https://doi.org/10.1007/s13206-022-00064-1.
Habchi, C., Harion, J.-L., Russeil, S., Bougeard, D., Hachem, F., Elmarakbi, A., 2013. Chem. Eng. Sci. 104, 439–450. https://doi.org/10.1016/j.ces.2013.09.032.
Han, W., Li, W., Zhang, H., 2024. Int. Commun. Heat Mass Tran. 157, 107843. https://doi.org/10.1016/j.icheatmasstransfer.2024.107843.
Han, W.(韩文博), Li, W.(李伟), Zhang, H.(张洪朋), 2024. Phys. Fluids 36, 101306. https://doi.org/10.1063/5.0238393.
Hessel, V., Löwe, H., Schönfeld, F., 2005. Chem. Eng. Sci. 60, 2479–2501. https://doi.org/10.1016/j.ces.2004.11.033.
Hu, Y., He, Z., Hao, Y., Gong, L., Pang, M., Howard, G.P., Ahn, H.-H., Brummet, M., Chen, K., Liu, H., Ke, X., Zhu, J., Anderson, C.F., Cui, H., Ullman, C.G., Carrington, C. A., Pomper, M.G., Seo, J.-H., Mittal, R., Minn, I., Mao, H.-Q., 2019. ACS Nano 13, 10161–10178. https://doi.org/10.1021/acsnano.9b03334.
Jain, B.P., Pandey, S., 2022. Academic Press. ISBN: 9780323998833.
Jiang, F., Drese, K.S., Hardt, S., Küpper, M., Schönfeld, F., 2004. AIChE J. 50, 2297–2305. https://doi.org/10.1002/aic.10188.
Kim, A., Ng, W.B., Bernt, W., Cho, N.-J., 2019. Sci. Rep. 9, 2639. https://doi.org/10.1038/s41598-019-38915-x.
Koohkansaadi, G., Mohagheghi, A., Mobed, A., Charsouei, S., 2025. Analyt. Sci. Adv. 6, e70035. https://doi.org/10.1002/ansa.70035.
Li, Z., Zhang, B., Dang, D., Yang, X., Yang, W., Liang, W., 2022. Sensor Actuator Phys. 344, 113757. https://doi.org/10.1016/j.sna.2022.113757.
Liu, K.-K., Wu, R.-G., Chuang, Y.-J., Khoo, H.S., Huang, S.-H., Tseng, F.-G., 2010. Sensors 10, 6623–6661. https://doi.org/10.3390/s100706623.
Materón, E.M., Miyazaki, C.M., Carr, O., Joshi, N., Picciani, P.H.S., Dalmaschio, C.J., Davis, F., Shimizu, F.M., 2021. Appl. Surf. Sci. Adv. 6, 100163. https://doi.org/10.1016/j.apsadv.2021.100163.
Mehta, P., Rahman, Z., ten Dijke, P., Boukany, P.E., 2022. Trends Cancer 8, 683–697. https://doi.org/10.1016/j.trecan.2022.03.006.
Mohanty, S.P., Kougianos, E., 2006. IEEE Potentials 25, 35–40. https://doi.org/10.1109/MP.2006.1649009.
Monopoli, M.P., Åberg, C., Salvati, A., Dawson, K.A., 2012. Nat. Nanotechnol. 7, 779–786. https://doi.org/10.1038/nnano.2012.207.
Nge, P.N., Rogers, C.I., Woolley, A.T., 2013. Chem. Rev. 113, 2550–2583. https://doi.org/10.1021/cr300337x.
Nguyen, N.-T., 2011. Imprint: William Andrew. ISBN: 9781437735215.
Nguyen, N.-T., Wu, Z., 2004. J. Micromech. Microeng. 15, R1.
Ozawa, M., Ozawa, T., Nishio, M., Ueda, K., 2017. J. Mol. Graph. Model. 75, 117–124. https://doi.org/10.1016/j.jmgm.2017.05.002.
Parvin, N., Joo, S.W., Jung, J.H., Mandal, T.K., 2025. Micromachines 16, 419. https://doi.org/10.3390/mi16040419.
Pennella, F., Mastrangelo, F., Gallo, D., Massai, D., Deriu, M.A., Labate, G.F.D., Bignardi, C., Montevecchi, F., Morbiducci, U., 2012. Single and Two-phase Flows on Chemical and Biomedical Engineering. Bentham Science Publishers, pp. 548–578.
Rodriguez-Loya, J., Lerma, M., Gardea-Torresdey, J.L., 2024. Micromachines 15, 24. https://doi.org/10.3390/mi15010024.
Saeed, M.M., Carthy, E., Dunne, N., Kinahan, D., 2025. Lab Chip 25, 3060–3093. https://doi.org/10.1039/D5LC00194C.
Saffar, Y., Kashanj, S., Nobes, D.S., Sabbagh, R., 2023. Micromachines 14. https://doi.org/10.3390/mi14122202.
Sanjay, S.T., Li, M., Zhou, W., Li, Xiaochun, Li, XiuJun, 2020. Microsyst. Nanoeng. 6, 28. https://doi.org/10.1038/s41378-020-0143-5.
Schneiderbauer, S., Krieger, M., 2013. Eur. J. Phys. 35, 015020. https://doi.org/10.1088/0143-0807/35/1/015020.
Shah, A., Srivastava, S., Chaturvedi, C.P., 2024. Clinical Applications of Biomolecules in Disease Diagnosis: a Comprehensive Guide to Biochemistry and Metabolism.
Shahidian, A., Tahouneh, S., 2025. Journal of Computational & Applied Research in Mechanical Engineering (JCARME). https://doi.org/10.22061/jcarme.2025.10035.2349.
Shi, J., Zhang, Y., Fan, Y., Liu, Y., Yang, M., 2024. Droplet 3, e92. https://doi.org/10.1002/dro2.92.
Soltani, D., Persoons, T., Alimohammadi, S., 2024. J. Micromech. Microeng. 34, 113001. https://doi.org/10.1088/1361-6439/ad809a.
Squires, T.M., Quake, S.R., 2005. Rev. Mod. Phys. 77, 977–1026. https://doi.org/10.1103/RevModPhys.77.977.
Stone, H.A., Stroock, A.D., Ajdari, A., 2004. Annu. Rev. Fluid Mech. https://doi.org/10.1146/annurev.fluid.36.050802.122124.
Suh, Y.K., Kang, S., 2010. Micromachines 1, 82–111. https://doi.org/10.3390/mi1030082.
Turner, A.P.F., 2013. Chem. Soc. Rev. 42, 3184–3196. https://doi.org/10.1039/C3CS35528D.
Vilanova, O., Martinez-Serra, A., Monopoli, M.P., Franzese, G., 2025. Frontiers in Nanotechnology, vol. 6, 2024.
Wu, L., Qu, X., 2015. Chem. Soc. Rev. 44, 2963–2997. https://doi.org/10.1039/C4CS00370E.
Yager, P., Edwards, T., Fu, E., Helton, K., Nelson, K., Tam, M.R., Weigl, B.H., 2006. Nature 442, 412–418. https://doi.org/10.1038/nature05064.
Yeo, L.Y., Chang, H.-C., Chan, P.P.Y., Friend, J.R., 2011. Small 7, 12–48. https://doi.org/10.1002/smll.201000946.
Yu, Q., Zhao, L., Guo, C., Yan, B., Su, G., 2020. Front. Bioeng. Biotechnol. 8, 2020.
Zhai, J., Liu, Y., Ji, W., Huang, X., Wang, P., Li, Y., Li, H., Wong, A.H.-H., Zhou, X., Chen, P., Wang, L., Yang, N., Chen, C., Chen, H., Mak, P.-I., Deng, C.-X., Martins, R., Yang, M., Ho, T.-Y., Yi, S., Yao, H., Jia, Y., 2024. Nat. Commun. 15, 4363. https://doi.org/10.1038/s41467-024-48616-3.
Zhang, Y., Li, M., Gao, X., Chen, Y., Liu, T., 2019. J. Hematol. Oncol. 12, 137. https://doi.org/10.1186/s13045-019-0833-3.
Zhou, Y., Tao, L., Qiu, J., Xu, J., Yang, X., Zhang, Y., Tian, X., Guan, X., Cen, X., Zhao, Y., 2024. Signal Transduct. Targeted Ther. 9, 132. https://doi.org/10.1038/s41392-024-01823-2.